PCCP

Accepted Manuscript

ROYAL SOCIETY OF CHEMISTRY

www.rsc.org/pccp

PCCP

ARTICLE

Electronic structure and optical properties of graphene/stanene heterobilayer

Received 00th January 20xx,
Accepted 00th January 20xx

DOI: 10.1039/x0xx00000x

www.rsc.org/

Xianping Chen[a,b,†] Ruishen Meng[a,†], Junke Jiang[b], Qiuhua Liang[b], Qun Yang[a], Chunjian Tan[b], Xiang Sun[a], Shengli Zhang[c], Tian-Ling Ren[d]

The structural, electronic and optical properties of graphene hybrid with stanene, the tin counterpart of graphene are investigated by means of density functional calculation with the inclusion of the band gap opening and enhanced visible light response. The lattice mismatch between graphene and stanene is taken into consideration and several stacking methods for model construction are proposed to study the possible effects. The Dirac feature can be observed in this bilayer system with relatively stronger interlayer interaction than weak van der Waals, which is ascribed to the unsaturated P orbital of stanene. Despite the mutual semi-metal nature of the graphene and stanene, it is also of significance to note that the band gap opening and the electrical neutrality of the bilayer. The combination of high carrier mobility of graphene and the excellent spin Hall effect of stanene is expected to coexist in the their bilayer structure. In addition, we found that the stanene monolayer has relatively lower work function than graphene and more importantly, it exhibits more pronounced optical adsorption capability than graphene. The results indicate that graphene/stanene heterobilayer will facilitate the performace of the stanene related spintronic devices and is a good candidate for photoelectronic devices.

1. Introduction

Since its first discovery in 2004[1], graphene has inspired tremendous research interests into the novel two-dimensional (2D) materials[2-5], in which special attention has been focused into the group-IV materials including silicene, germanene, and stanene which also inherit the exotic electronic properties of graphene. However, the mutual drawback of these 2D group-IV materials is the absence of band gap which give rise to their poor performance in the field effective transistor (FET) applications. The alternative way to solve this issue is the realization of heterostructures that are expected to combine the materials with various properties by mechanical stacking or epitaxial growth. This technic allows for atomically precise fabrication of novel structures that the unusual properties together with new phenomenon can be observed[6-10]. It has been theoretically reported or experimentally confirmed that the combinations of graphene/silicene with semiconductor[11-14] (TMCs including MoS_2, $MoSe_2$; C_3N_4, BC_3, etc.) or insulator [15-17](SiO_2, SiC, HfO_2, etc.) substrates would bring about band gap opening of 2-160 meV with the preservation of the Dirac cone. Besides, the graphene incorporated with nanoparticles[18-23] like TiO_2, ZnO, CeO_2, MnO_2 and CdS, etc. shows enhanced capability for catalytic, fuel cell, capacitor applications. In a nutshell, heterostructures holds great promise and potentials in diverse applications.

Recently, the monolayer stanene was experimentally fabricated by molecular beam epitaxy growth[24], which spurs further experimental investigation of its unique theoretically predicted properties, such as the disspationless electric conduction at room temperature ascribed to the large-gap 2D quantum spin Hall (QSH) state[25] making it an excellent topological insulator. Besides, stanene also possesses topological superconductivity as well as quantum anomalous Hall[26] (QAH) effects near room temperature. However, the investigation about its optical response is lacking. In this work, electronic structure and optical properties of graphene/stanene nanocomposites have been investigated via first principles calculations. Several representative models are proposed to investigate the influence of different stacking methods on the relevant properties of the bilayer. The band gap opening of the hybrid system is observed with the Fermi level of it located in the gap, and the Dirac feature is reappeared with the proper configuration construction and the high carrier mobility of graphene can be maintained. The imaginary part of the dielectric function is predicted for the graphene, stanene monolayer and the nanocomposites. We find that the stanene has more pronounced optical response than graphene. While the

[a] Faculty of Electromechanical Engineering, Guilin University of Electronic Technology, 541004 Guilin, China. E-mail: xianpingchen1979@126.com
[b] Key Laboratory of Optoelectronic Technology & Systems, Education Ministry of China, Chongqing University, and College of Opto-electronic Engineering, Chongqing University, 400044 Chongqing, China.
[c] Institute of Optoelectronics & Nanomaterials, College of Materials Science and Engineering, Nanjing University of Science and Technology, Nanjing 210094, China. E-mail: zhangslvip@njust.edu.cn
[d] Institute of Microelectronics, Tsinghua University, 100084 Beijing, China.
† These authors contributed equally to this work.
Electronic Supplementary Information (ESI) available: [details of any supplementary information available should be included here]. See DOI: 10.1039/x0xx00000x

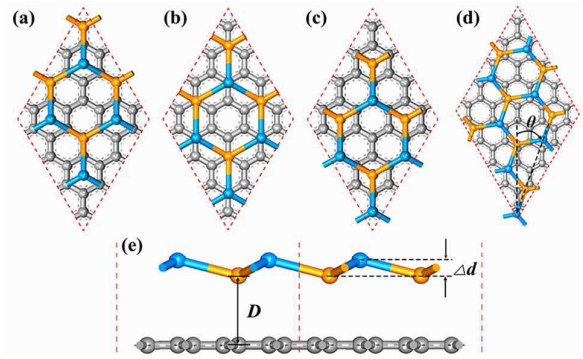

Fig. 1. Top view of the atomic model of the graphene/stanene heterobilayer: (a) Pattern i, (b) Pattern ii, (c) Pattern iii of the G(4)/Sn(2) supercell, (d) G(5)/Sn(√7) supercell, θ is the rotational angle between two layers. (e) is the side view of the graphene/tanene bilayer. D denotes interlayer distance, Δd is the buckling height of the stanene layer. The C atom of the graphene, and the Sn atoms in upper/lower level are represented by grey, blue and yellow balls respectively. The unit cells are shown in red dashed lines.

nanocomposites may exhibit enhanced response in the visible light region. We believe that the experimental realization of this heterobilayer will be benefit from the compatibility with conventional semiconductor process.

2. Computational methods

In the present work, the first principle calculations were performed using density functional theory (DFT) including in DMOL^3 package[27-30]. The generalized gradient approximation (GGA) with Perdew-Burke-Ernzerhof (PBE) exchange-correlation functional was used to describe the exchange-correlation interaction. To take the van der Waals (vdW) into consideration, DFT-D (D stands for dispersion) method proposed by Grimme[31] was used through all calculations. To evaluate the reliability of the DFT-D method, the benchmark calculation is carried out and it gives the interlayer distance of 3.344 Å and binding energy (E_b) of 31.7 meV for the bilayer graphene, which correspond well with the experimental results[32] (c= 3.35 Å and E_b = −26 meV) and theoretical investigations[33, 34] (c= 3.34 Å and E_b = −31 meV). Besides, double numerical atomic orbital plus polarization (DNP) was chosen as the basis set with the global cutoff of 4.9 Å to ensure the high computational quality. The K points of 20×20×1 was set for the geometry optimization and 30×30×1 for accurate electric characteristics calculations, and the smearing value was 0.002 Ha (1Ha = 27.2114 eV). Moreover, the atomic positions and cell vectors are relaxed until the energy, maximum force and maximum displacement are less than 10^{-6} Ha, 0.0015 Ha/Å, and 0.003 Å, respectively. Furthermore, a vacuum space larger than 20 Å was utilized to prevent the interactions between neighbouring layers in the direction normal to the graphene and stanene surface. The optical properties were calculated in CASTEP code[35], with a plane-wave kinetic energy cutoff of 300 eV, and the K point mesh was set to 8×8×1 considering the limited computational resources.

The lattice constant, buckling height and the Sn-Sn bond length of the stanene after the geometry optimization in our calculation are 4.669 Å, 0.888 Å and 2.839 Å respectively, which is similar to the previous theoretical[36] and experimental studies[24]. Besides, the optimized lattice constant of the graphene is 2.46 Å, so we proposed two appropriate supercells for the graphene/stanene bilayer system, namely, the supercell composed of 4×4 graphene and 2×2 stanene (G(4)/Sn(2)), and the other supercell made up of 5×5 graphene and √7×√7 stanene (G(5)/ Sn (√7)). It should be pointed out that, graphene is subjected to strains to adjust the lattice constant of the other layer to form commensurability structures in many heterostructure investigations[11, 14, 37, 38], however, the possible consequences are deserved to be further studied. According to the dissimilarity of the lattice parameters, the G(4)/Sn(2) supercell would inevitably result in the lattice mismatch amounted to 4.7%, therefore we have to carry out three commensurability conditions marked as A, B and C to take the possible effects into deeper consideration. In the A situation, the in-plane lattice constant of the bilayer supercell is set as the lattice constant of single-layer stanene, which would introduce a homogeneous compressive strain of 4.7% to graphene. In the B situation, the lattice constant of stanene is adjusted to adapt the one of graphene, concomitantly, and the stanene monolayer is stretched by 4.7%. With respect to the C situation, we choose the average lattice constant of two layers, which means the ratio of the elongation as well as the compression of them is identical (~2.38%). Meanwhile, three stacking patterns of the G(4)/Sn(2) supercell denoted as i, ii and iii are shown in Figs. 1(a), (b) and (c) respectively. As for the G(5)/Sn (√7) bilayer shown in Fig. 1(d), the appropriate supercell is constructed by rotating the stanene with respect to graphene. The base vectors of graphene and stanene primitive cells without rotation are[39-41]:

$$\vec{a}_1 = (\sqrt{3}/2, -1/2)u \qquad \vec{a}_2 = (\sqrt{3}/2,\ 1/2)u$$
$$\vec{b}_1 = (\sqrt{3}/2, -1/2)v \qquad \vec{b}_2 = (\sqrt{3}/2,\ 1/2)u$$

in which u and v are the lattice constant of graphene and stanene. The base vector of the graphene/stanene supercell is defined as:

$$\vec{A}_1 = n\vec{a}_1 + m\vec{a}_2 \qquad \vec{A}_2 = -m\vec{a}_1 + (m+n)\vec{a}_2$$

The new supercell of the stanene must be rebuilt to match the lattice of graphene, with its base vector given as:

$$\vec{c}_1 = s\vec{b}_1 + t\vec{b}_2 \qquad \vec{c}_2 = -t\vec{b}_1 + (s+t)\vec{b}_2$$

Then the rotation angle θ to realize the coincidence of $\vec{A}_1$ and $\vec{c}_1$, $\vec{A}_2$ and $\vec{c}_2$ can be calculated as:

$$\cos\theta = \frac{\vec{A}_1 \cdot \vec{c}_1}{|\vec{A}_1| \times |\vec{c}_1|} = \frac{ns + mt + (ms+nt)/2}{\sqrt{m^2+n^2+mn} \times \sqrt{s^2+t^2+st}}$$

Accordingly, the calculated rotation angle is 19.1° with a very tiny lattice mismatch less than 0.5%, which is small enough that adapting the lattice constant of graphene to the stannene would not lead to notable effects on the results. The lattice constants of the supercells were kept fixed to maintain the original structure for investigation during the optimization process. Alternatively, the optimized-cell option (the cell parameters

will be optimized during the geometry optimization) was also carried out for comparison.

Table 1 Structure/electronic properties of G(4)/Sn(2) with i, ii, iii pattern and G(5)/Sn($\sqrt{7}$), including the distance between the lower Sn atom to the graphene plane (D), binding energy per Sn atom (Eb), band gap (Eg) and charge transfer (ΔQ) by Hirshfeld method, the positive signs denote that the charges transfer from stanene to graphene.

Configuration /Pattern		D (Å)	E_b (meV)	E_g (meV)	ΔQ (e)
A	i	3.355	-206	91	0.145
	ii	3.300	-215	88	0.152
	iii	3.305	-213	71	0.162
B	i	3.381	-185	120	0.176
	ii	3.302	-190	77	0.190
	iii	3.332	-189	47	0.182
C	i	3.373	-195	123	0.157
	ii	3.307	-199	113	0.167
	iii	3.325	-198	82	0.162
G(5)/ Sn($\sqrt{7}$)		3.323	-182	30	0.279

To calculate the optical properties of graphene/stanene bilayer, the frequency-dependent dielectric matrixes are determined by the Fermi golden rule within the dipole approximation. The imaginary part of the dielectric function due to the occupied and unoccupied electronic states can be expressed as[42]:

$$\varepsilon_2(\hbar\omega) = \frac{4\pi^2 e^2}{\Omega\varepsilon_0}\sum_{c,v,k}|<\psi_k^c|u\cdot r|\psi_k^v>|^2\delta(E_k^c - E_k^v - E)$$

where Ω is the unit-cell volume, ω is the photon frequency, u is the vector defining the polarization of the incident electric field, c and k represent the conduction band and valence band, respectively. Via the Kramers-Kronig relations, the real part ε_1 of the dielectric function is obtain from ε_2. Other optical properties such as absorption coefficient can be gained by the following equation[43]:

$$\alpha(\omega) = \sqrt{2}\omega[\sqrt{\varepsilon_1^2(\omega)+\varepsilon_2^2(\omega)} - \varepsilon_1(\omega)]^{1/2}$$

To quantitatively evaluate the interaction intensity, the binding energies (E_b) per Sn atom are calculated as,

$$E_b = (E_{G/S} - E_G - E_S)/N$$

where $E_{G/S}$ is the total energy of the graphene/stanene bilayer, E_G and E_S are the energies of the isolated graphene and stanene monolayer with the same structure as they are in the corresponding heterobilayer[37, 44], N is the number of the Sn atoms. It should be clarified that the E_G are different from each other in different commensurability situations in which the graphenes undergo different strains, so are the E_S. Therefore, the E_b can't be the criterion of the stability for the bilayer in contrast to $E_{G/S}$.

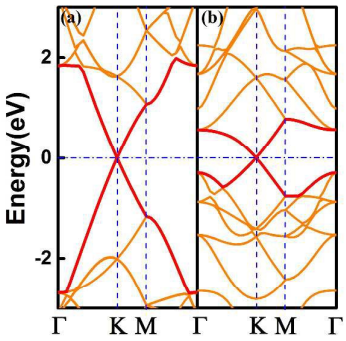

Fig 2. The band structure of: pristine (a) graphene; (b) stanene.

3. Results and discussion

The optimization results suggest that the graphene/stanene layer structure is stable with no distortion on structure. The lattice parameters and the relevant electronic properties of the graphene/stanene bilayers are concluded in Table 1. The result of the energy relaxation turns out that the configurations with pattern ii in the G(4)/Sn(2) supercells have the lowest binding energies, shortest interlayer distance as well as the almost highest charge transfer[45] in comparison with the i and ii patterns. So in the following calculations, we only consider this energetically favourable pattern in which every hexagonal Sn atom ring of stanene embraces a benzenoid ring of graphene and every Sn atom is on the top of the C atom. Although A configurations have the lowest E_b, the B configurations have the lowest total energies, followed by the C configurations. Furthermore, both the Aii and Cii configurations transformed to Bii configuration if the optimize-cell option is taken into account in the geometry optimization calculation, further suggesting that the B configurations are the most stable ones thus we mainly focus on the Bii configuration for the G(4)/Sn(2) bilayers. The band structures of the optimized free-standing graphene and

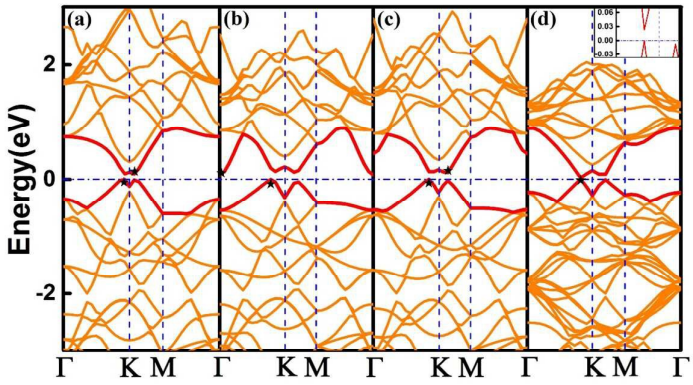

Fig 3. The band structures of (a) Aii, (b)Bii, (c)Cii patterns of G(4)/Sn(2), and (d) G(5)/ Sn($\sqrt{7}$) heterobilayer. (Insets) Magnification of the conical point around K point near the Fermi levels.The CBM and VBM are marked with black stars.

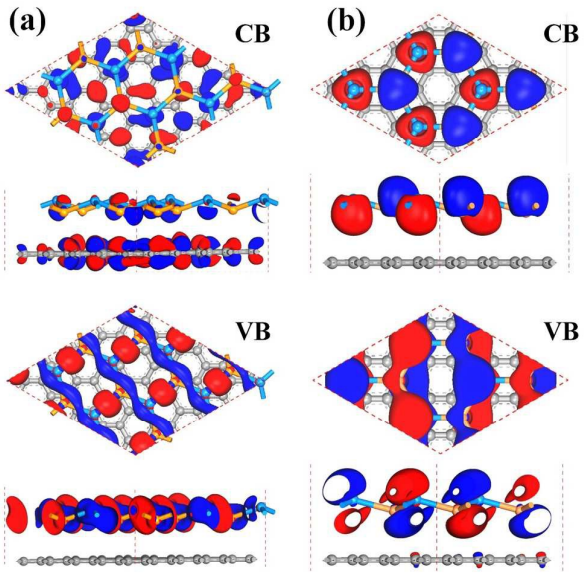

Fig. 4. The real-space charge distribution valence band and conduction band of G(5)/Sn(√7) and Bii configuration at Γ point. The isovalue is 0.02 e/Å3. The blue and red color represent different signs of the wave function.

stanene are given in Fig 2(a) and (b) respectively, where the filled-state π and empty state π* bands of graphene touch each other at the high-symmetry K point (Dirac point) of the Brillouin zone (BZ) on the Fermi level (E_F) in formation of the Dirac cone, resulting in the gapless semi-metal nature. In addition, pristine stanene shares the similar Dirac feature and no band gap is observed in absence of the spin orbital coulping (SOC) effect. Nevertheless, something interesting happens when the hybrid graphene/stanene structure is taken shaped, that is, the band gap will be opened on the E_F, as can be seen in Fig 3. Compared with the band structures of the free-standing graphene and stanene, remarkable changes occur in the top valence bands and the bottom conduction bands of G(4)/Sn(2) bilayers, in which the former CBM and VBM seem like repulsing each other, and symmetrically shift to the points near the K point in the two-dimensional hexagonal BZ. Consequently the Dirac point is perturbed, giving rise to the indirect band gap opeing of 88, 77 and 113 meV for the Aii, Bii and Cii configurations respectively. Moreover, the locations of the VBMs are robust irrespective of the commensurability conditions, while the CBMs are susceptible to them. It is clear to see from the Figs. 3(a), (b) and (c) that the VBMs of the Aii and Cii configurations are located near the K point of the BZ, while the VBM of the Bii configuration shifts to the Γ point. This result indicates that the commensurability condition would play an important role in determining the electronic properties of the graphene/stanene heterostructure. As for the band structure of G(5)/Sn(√7) plotted in Fig. 3(d), the VBM lies in the nearby position of the K point similar to that of the G(4)/Sn(2) bilayer, whereas the CBM locates in the corresponded position on the opposite side of the E_F, giving rise to the reemergence of the Dirac feature with the direct band gap of 30 meV on the E_F. In addition, it is of significance to find that all the highest valence bands and lowest conduction bands in the bilayer system is broad with comparison to that of the stanene, indicates the strong electron delocalization. Particularly, the curvature of the lowest conduction band in the G(5)/Sn(√7) bilayer is even larger than the one of stanene. As the effective mass is inversely proportional to the band curvature, a higher charge carrier mobility can be expected for the G(5)/Sn(√7) bilayer. From the stanene point of view, the interlayer interactions will modulate and facilitate the electronic properties as supported by the real space charge density distributions shown in Fig. 4 (a). The valence band of the G(5)/Sn(7) bilayer is completely localized in the stanene layer and contributed by the Sn- Sn bond, showing a σ bond characteristics. While the conduction band is contributed by both graphene and stanene, and representing the π bond feature, which indirectly demonstrates the effects that interlayer interaction has on the band structure. In regard to the Bii configuration of the G(4)/Sn(2) bilayer, the valence band together with conduction band is almost all localized on the stanene, implying that stanene is responsible for the electronic property of the G(4)/Sn(2) structure that the variation of the CBM locations in different configurations can be ascribed to the extra strains applied to the corresponding stanene monolayer.

To gain deeper insight into the electronic properties, it is worth to investigate their interlayer interactions. In the graphene/semiconductor[14, 38, 46, 47] graphene/insulator[16, 48] hybrid systems dominated by the weak van der Waals interaction, their band structures are mainly the simple sum of those of each constituent, where the π and π* bands with linear dispersion filled in the band gap of the substrate and the magnitude of binding energies are typically lower than 100 meV per C atom. However, in the graphene/metal (Co, Ni or Pd) hybrid systems[37, 49-51] in formation of stronger covalent bonds, the graphene bands are significantly perturbed and the Dirac cones are completely destroyed, finally acquire a mixed graphene-metal character due to the significant interaction[51]. When the graphenes are adsorbed on the metal layers (Al, Ag or Pt) with weaker interaction, their conical points at the K point can still be observed but the bands will upshift or downshift crossing the E_F, exhibiting the doping characteristics. On contrary, in graphene/stanene heterobilayer structures, the electrical neutrality are kept, where the E_F lies in the gap, contrasting to the graphene/silicene and graphene/germanene hybrid bilayers[39]. Besides, the optimal interlayer distances in graphene/stanene bilayers are equal or greater than 3.300 Å, which is obviously larger than the typical lengths of the Sn-C bonds[52] and the sum of the

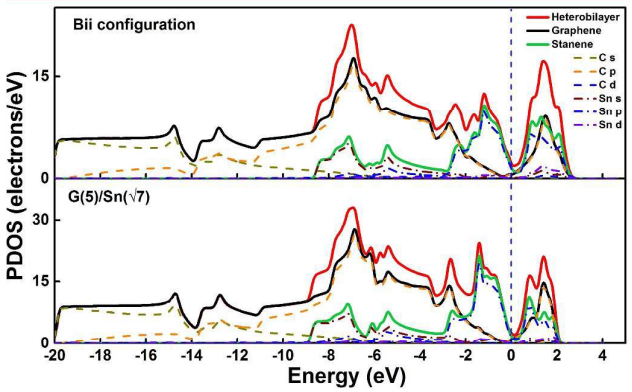

Fig. 5. The density of states for the Bii configuration (upper) and the G(5)/Sn(√7) (bottom) heterobilayers. The Fermi level is set to 0.

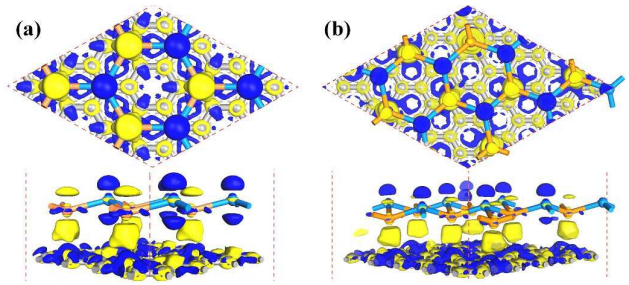

Fig. 6. The charge density difference of the Bii configuraion (a) and the G(5)/Sn(√7) bilayer. Blue and yellow respectively represent charge accumulation and depletion in the space with respect to isolate graphene and stanene. The isovalue is chosen to be 0.002 e/Å^3.

covalent radii[53] of the Sn and C atoms, indicating the absence of Sn-C covalent bonds in the hybrid structures. What's more, the calculated binding energies per Sn atom at the optimum spacing is more than 180 meV, higher than the typical binding energies of the weak vdW interactions, suggesting that the stanene and graphene are bound to each other via other mechanism, for example, orbital hybridization or electrostatic interaction[17] instead of weak vdW interaction. In other words, the interfaces between the single-layer graphene and stanene are more energetically stable and easier to realize in experiment.

To shed more light on the interlayer interaction along with electronic characteristics, the total and atom projected density of states (PDOS) of G(5)/Sn(√7), and the Bii configuration of G(4)/Sn(2) are plotted in Fig 5, from which we can conclude that the PDOSs of isolated graphene and stanene originated from the hybrid system are very similar to that of the pristine ones unlike the hybrid system with strong chemical interaction[54], which means that the interactions are not rather intensive, so their electronic properties could be preserved in some extent. Clearly, the electronic states in the characteristic peaks in the conduction band (-2 to 0 eV) of the heterobilayers are predominantly contributed by the stanene, which is consistent with the real space charge density distributions in the Fig. 5. Besides, the peaks on the conduction band (0-2 eV) consist of both graphene and stanene states, which are dominated by their p orbitals. Doubtlessly, the role that P orbital of stanene (Sn p) plays is prominent not only in the electric properties but also in the stability of the bilayer system because of its unsaturated nature which lead to a strong chemical activity. As we can see from the PDOS that the C s and Sn p, the Sn s and C p orbitals of the G(5)/Sn(√7) structure respectively share the similar states within the range of -8 to -6 eV and -1 to 0 eV, indicating the slight orbital hybridization, eventually lead to higher binding energy as well as larger Mulliken charge transfer compared with the vdw hybrid systems. We also plotted the charge density difference (CDD) of the G(5)/Sn (√7) structure and the Bii configuration for G(4)/Sn(2) in Fig. 6, which can be expressed as:

$$\Delta\rho = \rho_{G/S} - \rho_G - \rho_S$$

Where $\rho_{G/S}$, ρ_G and ρ_S are the total charge density of the heterobilayers, isolated graphene and stanene monolayer in the corresponding heterobilayer, respectively. The CDDs of G(4)/Sn(2) and G(5)/Sn (√7) share the similar features. It is of significance to find that the evident charge rearrangement localized at the interlayer region, which is the result of the orbital overlaps. In addition, the electrons are depleted on the lower Sn atoms and the C atoms while the majority of them are accumulated at the upper Sn atoms, that is to say, large charge transfer occurs between the sublattice of the stanene, leading to the broken of symmetry. The calculated Mulliken charges transfer from stanene to graphene, arising from the unsaturated P orbital except for the A configuration. The Mulliken charges in the B configurations of G(4)/Sn(2) are nearly three times higher than that of the A and C configurations, further hindering the higher stability.

The work functions (WF) and optical properties of the graphene/stanene bilayer are calculated to explore its possible applications in field emission and the photo-related fields. The WFs are calculated by aligning the Fermi level corresponded to the vacuum level, which have been performed in the graphene heterostructure[38, 47, 55]. The obtained WF for graphene is 4.57 eV, which is comparable to the experimental results[56] and theoretical calculation[49]. In addition, the calculated WF of the stanene is 4.22 eV, lower than the experimental measurement of the bulk tin (4.32 eV). While the calculated WF for the graphene/stanene bilayer is 4.43 eV, a little weaker than that of graphene. The external field (E-Field) with its direction vertical to the infinite plane of the bilayer was introduced to the G(5)/Sn(√7) bilayer to investigate its effects on the electronic

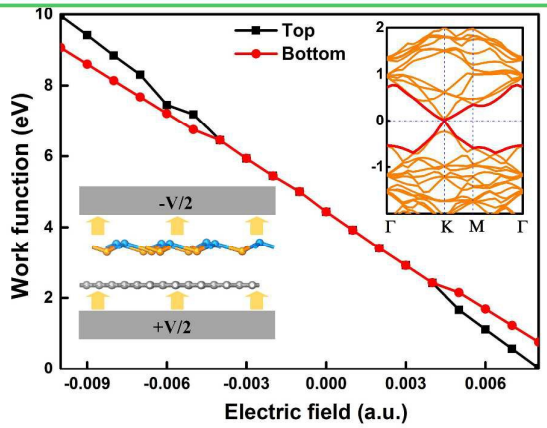

Fig. 7. The calculated work function of the G(5)/Sn(√7) as a function of applied electric field. (bottom inset) The positive direction of the electric field is pointed by the yellow arrows from graphene to stanene. The infinite plane of graphene/stanene bilayer is perpendicular to the electric field. (Upper inset) The band structure of G(5)/Sn(√7) under the 0.003 a.u.

properties. The direction of the E-Field is shown in the inset of Fig. 7. Under the negative external electric field, the band gap increases to 59 meV at first, then vanishes at a very tiny intensity of ~ -0.002 a.u. because the lowest conduction band will down shifted and penetrates the E_F. When the positive electric field is applied, the band gap values would oscillate irrespective of the field intensity. However, it is very interesting to find that both the CBM and VBM shift to the K point of the BZ, with the the very tiny band gap of 12 to 13 meV when the

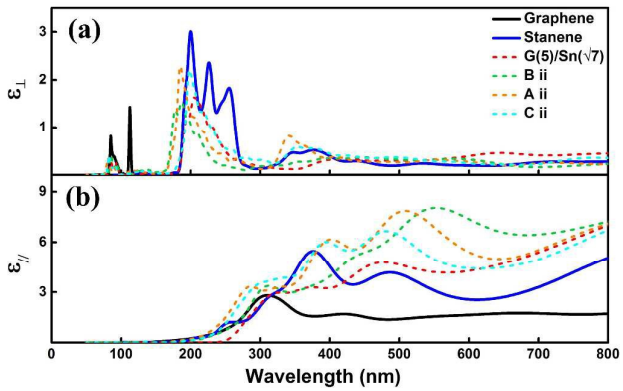

Fig 8. The calculated imaginary part of dielectric function for the G(4)/Sn(2) and G(5)/Sn(√7) bilayer with the polarization vector perpendicular (a) and parallel (b) to the surface.

field intensity reaches 0.003 to 0.004 au, lead to the graphene-like Dirac cone emerging in the heterobliayer as show in the upper-right insert in Fig. 7. The highest valence band is broader and the highest conduction band is smoother due to the charge rearrangement induced by the E-Field. In other word, the higher carrier mobility is ensured. It is worth to investigate the spin Hall effect and evaluate the possible applications in the spintronic devices in view of the intriguing phenomenon in the graphene/stanene bilayer. Furthermore, Fig. 7 also shows the WFs as a function of the E-Field, from which we can see the negative relationship between the WFs and the positive E-field intensity. Besides, the WFs increase with the increase of negative E-field, showing that WF is a linear function of the applied E-Field. The work function of the heterostructure will split into two values of the bottom layer and the top layer when the E-Field is stronger than 0.005 a.u. or -0.005 a.u. This wide range of adjustable work function enables the graphene/bilayer bilayer to be a suitable material for field-emitted devices.

The optical properties of the graphene/stanene bilayers are discussed on the basis of the dielectric function with comparison to the one of pure graphene and stanene monolayer. The imaginary parts of dielectric function under parallel ($\varepsilon_{\perp}$) and perpendicular ($\varepsilon_{\parallel}$) polarization are taken into account. Considering the underestimation of band gap in the DFT calculation, the adsorption edges of these curves should have a red shift about 150 nm[57]. For the perpendicular polarization, as shown in Fig. 8 (a), the calculated $\varepsilon_{\perp}$ of graphene is similar to that of the calculated result of Hu *et at.*[54], indicating our calculation is reasonable. Contrast to graphene which only exhibits short-wavelength light adsorption, stanene has more pronounced UV adsorption ranged from 200-300 nm. Therefore, the UV light and visible light response of stanene are more effective and it displays great potential in the photo-related applications with the consideration of its low work function. The general tendencies of the $\varepsilon_{\perp}$ for G(4)/Sn(2) and G(5)/Sn(√7) bilayers are similar and all of these structures and shows narrowed adsorption feature in the range of 100-280 nm. While the slightly enhanced adsorption in the visible light region is observed compared with their isolated constituents. For parallel polarization shown in Fig. 8 (b), all these structures exhibit enhanced light adsorption from far ultraviolet to visible light region. Likewise, the overall adsorption profile of stanene is higher than that of the graphene. It should be noted that the enhanced optical performance of all the heterobilayers is clear, and most of them display more prominent visible light response in the region from 400 nm to 800 nm. As has been verified in many previous research works[58, 59] that the interlayer coupling plays a very important role in modifying the optical properties of the hybrid system. The enhanced optical absorption of the graphene/stanene heterobilayer in the wavelength range larger than 400 nm (lower than 3 eV) is mainly due to the electronic state overlaps. This phenomenon can be found in the PDOS that the electronic states around the Fermi level are dominated by the stanene, which facilitates the transition between C 2p state of graphene and Sn 2p state of stanene. Therefore, the direct electrons excitation can occur between graphene and stanene. Concomitantly, the hybrid graphene/stanene nanostructure may be expected to display enhanced photoresponse under the visible light irradiation, which shows their potential in photo-related application prospect.

Conclusions

In summary, we have performed density functional calculations to study the electronic and optical properties of the graphene/stanene heterobilayers in different commensurabilities. The interactions between graphene and stanene monolayer are relatively stronger than the weak van der waals effect which would improve the stability because of the slight orbital hybridization caused by the chemically active stanene layer. The Dirac cone is disturbed in the G(4)/Sn(2) bilayers which give rise to the indirect band gaps opening around 80 meV. On the contrary, in the G(5)/Sn(√7) bilayer, the Dirac feature is observed with its CBM and VBM located at the positions next to the high symmetry K point of the Brillouin zone. Excitingly, the lowest conduction band curve is even larger than that of the pristine stanene. What's more, the introduction of the external electric field will shift the positions of the CBM and VBM to the K point of the BZ, leading to a graphene-like Dirac cone emerging, eventually, high charge carrier mobility is expected in the heterobilayer. This interesting phenomenon would pave a way for the investigation of the QSH insulator and high-speed spintronics devices. Furthermore, the calculated work function of the bilayer is 4.43 eV, lower than graphene, and it can be modulated by the external electric field, indicating the potential of the graphene/stanene bilayer in the field-emitted devices. For optical properties, both the G(4)/Sn(2) and G(5)/Sn(√7) bilayers show enhanced visible light absorption, this unique and tunable optical properties of graphene/stanene heterostructure implicate the applications on the spintronic devices and the photoelectric devices.

Acknowledgements

The research is co-supported by National Natural Science Foundation of China under Grant No. 51303033, the Guangxi Natural Science Foundation under Grant No. 2014GXNSFCB118004, the Guilin Science and Technology Development Foundation under Grant No. 20140103-3, and the Guangxi Universities' Scientific Foundation under Grant No. YB2014116.

Notes and references

1 K.S. Novoselov, A.K. Geim, S.V. Morozov, D. Jiang, Y. Zhang, S.V. Dubonos, I.V. Grigorieva and A.A. Firsov, *Science*, 2004, **306**, 666-669.

2 M.S. Xu, T. Liang, M.M. Shi and H.Z. Chen, *Chemical reviews*, 2013, **113**, 3766-3798.

3 P. Miró, M. Audiffred and T. Heine, *Chemical Society Reviews*, 2014, **43**, 6537-6554.

4 S.L. Zhang, Z. Yan, Y.F. Li, Z.F. Chen and H.B. Zeng, *Angewandte Chemie International Edition*, 2015, **54**, 3112-3115.

5 S.L. Zhang, M.Q. Xie, F.Y. Li, Z. Yan, Y.F. Li, E.J. Kan, W. Liu, Z.F. Chen and H.B. Zeng, *Angewandte Chemie*, 2016, **128**, 1698-1701.

6 H. Zhang, Y.N. Zhang, H. Liu and L.M. Liu, *Journal of Materials Chemistry A*, 2014, **2**, 15389.

7 A.K. Geim and I.V. Grigorieva, *Nature*, 2013, **499**, 419-425.

8 W. Hu and J.l. Yang, *Computational Materials Science*, 2016, **112**, 518-526.

9 T.c. Niu and A. Li, *Progress in Surface Science*, 2015, **90**, 21-45.

10 H. Wang, F. Liu, W. Fu, Z. Fang, W. Zhou and Z. Liu, *Nanoscale*, 2014, **6**, 12250-12272.

11 S.S. Li, C.W. Zhang, W.X. Ji, F. Li and P.J. Wang, *Physical chemistry chemical physics : PCCP*, 2014, **16**, 22861-22866.

12 W. Zan, W. Geng, H. Liu and X. Yao, *Physical chemistry chemical physics : PCCP*, 2016, **18**, 3159-3164.

13 H.C. Diaz, J. Avila, C. Chen, R. Addou, M.C. Asensio and M. Batzill, *Nano letters*, 2015, **15**, 1135-1140.

14 X. Li, Y. Dai, Y. Ma, S. Han and B. Huang, *Physical chemistry chemical physics : PCCP*, 2014, **16**, 4230-4235.

15 T.C. Nguyen, M. Otani and S. Okada, *Physical review letters*, 2011, **106**, 106801.

16 L. Magaud, F. Hiebel, F. Varchon, P. Mallet and J.Y. Veuillen, *Physical Review B*, 2009, **79**, 161405.

17 K. Kamiya, N. Umezawa and S. Okada, *Physical Review B*, 2011, **83**, 153413.

18 L. Jing, Z.Y. Yang, Y.F. Zhao, Y.X. Zhang, X. Guo, Y.M. Yan and K.N. Sun, *J. Mater. Chem. A*, 2014, **2**, 1068-1075.

19 S.Y. Yin, X.J. Men, H. Sun, P. She, W. Zhang, C.F. Wu, W.P. Qin and X.D. Chen, *J. Mater. Chem. A*, 2015, **3**, 12016-12022.

20 X. Wang, X. Li, D. Liu, S. Song and H. Zhang, *Chemical communications*, 2012, **48**, 2885-2887.

21 X.M. Feng, Z.Z. Yan, N.N. Chen, Y. Zhang, Y.W. Ma, X.F. Liu, Q.L. Fan, L.H. Wang and W. Huang, *Journal of Materials Chemistry A*, 2013, **1**, 12818.

22 S.Q. Liu, M.Q. Yang and Y.J. Xu, *J. Mater. Chem. A*, 2014, **2**, 430-440.

23 Z.Y. Ren, J.Y. Zhang, F.X. Xiao and G.C. Xiao, *Journal of Materials Chemistry A*, 2014, **2**, 5330.

24 F.F. Zhu, W.J. Chen, Y. Xu, C.L. Gao, D.D. Guan, C.H. Liu, D. Qian, S.C. Zhang and J.F. Jia, *Nature materials*, 2015, **14**, 1020-1025.

25 Y. Xu, B. Yan, H.J. Zhang, J. Wang, G. Xu, P. Tang, W. Duan and S.C. Zhang, *Physical review letters*, 2013, **111**, 136804.

26 S.C. Wu, G. Shan and B. Yan, *Physical review letters*, 2014, **113**, 256401.

27 B. Delley, *The Journal of chemical physics*, 2000, **113**, 7756-7764.

28 X.P. Chen, N. Yang, J.M. Ni, M. Cai, H. Ye, C.K. Wong, S.Y. Leung and T.L. Ren, *Electron Device Letters, IEEE*, 2015, **36**, 1366-1368.

29 X.P. Chen, J.K. Jiang, Q.H. Liang, N. Yang, H.Y. Ye, M. Cai, L. Shen, D.G. Yang and T.L. Ren, *Scientific reports*, 2015, **5**, 16907.

30 X.P. Chen, Q.H. Liang, J.K. Jiang, C.K. Wong, S.Y. Leung, H.Y. Ye, D.G. Yang and T.L. Ren, *Scientific reports*, 2016, **6**, 20621.

31 S. Grimme, *Journal of computational chemistry*, 2006, **27**, 1787-1799.

32 R. Zacharia, H. Ulbricht and T. Hertel, *Physical Review B*, 2004, **69**, 155406.

33 W. Hu, Z.y. Li and J.l. Yang, *The Journal of chemical physics*, 2013, **138**, 054701.

34 R.E. Mapasha, A.M. Ukpong and N. Chetty, *Physical Review B*, 2012, **85**, 205402.

35 M. Segall, P.J. Lindan, M.a. Probert, C. Pickard, P. Hasnip, S. Clark and M. Payne, *Journal of Physics: Condensed Matter*, 2002, **14**, 2717.

36 J.C. Garcia, D.B. de Lima, L.V.C. Assali and J.o.F. Justo, *The Journal of Physical Chemistry C*, 2011, **115**, 13242-13246.

37 I. Hamada and M. Otani, *Physical Review B*, 2010, **82**, 153412.

38 X.E. Liu and Z.Y. Li, *The Journal of Physical Chemistry Letters*, 2015, **6**, 3269-3275.

39 Y.m. Cai, C.P. Chuu, C.M. Wei and M.Y. Chou, *Physical Review B*, 2013, **88**, 5647-5654.

40 G.T. De Laissardire, D. Mayou and L. Magaud, *Nano letters*, 2009, **10**, 804-808.

41 J.M. Campanera, G. Savini, I. Suarez-Martinez and M.I. Heggie, *Physical Review B*, 2007, **75**, 235449.

42 M. Gajdoš, K. Hummer, G. Kresse, J. Furthmüller and F. Bechstedt, *Physical Review B*, 2006, **73**, 045112.

43 S. Saha, T. Sinha and A. Mookerjee, *Physical Review B*, 2000, **62**, 8828.

44 L.y. Li and M.w. Zhao, *The Journal of Physical Chemistry C*, 2014, **118**, 19129-19138.

45 F.L. Hirshfeld, *Theoretica chimica acta*, 1977, **44**, 129-138.

46 Y. Ma, Y. Dai, M. Guo, C. Niu and B. Huang, *Nanoscale*, 2011, **3**, 3883-3887.

47 W. Geng, X.f. Zhao, H.x. Liu and X.j. Yao, *The Journal of Physical Chemistry C*, 2013, **117**, 10536-10544.

48 C.R. Dean, A.F. Young, I. Meric, C. Lee, L. Wang, S. Sorgenfrei, K. Watanabe, T. Taniguchi, P. Kim and K.L. Shepard, *Nature Nanotechnology*, 2010, **5**, 722-726.

49 G. Giovannetti, ., P.A. Khomyakov, G. Brocks, ., V.M. Karpan, J. Brink, Van Den and P.J. Kelly, *Physical review letters*, 2008, **101**, 1676-1686.

50 M. Vanin, J.J. Mortensen, A.K. Kelkkanen, J.M. Garcia-Lastra, K.S. Thygesen and K.W. Jacobsen, *Physical Review B*, 2010, **81**, 081408.

51 M. Houssa, B. van den Broek, E. Scalise, G. Pourtois, V.V. Afanas'ev and A. Stesmans, *Physical chemistry chemical physics : PCCP*, 2013, **15**, 3702-3705.
52 U. Schubert, S. Grubert, U. Schulz and S. Mock, *Organometallics*, 1992, **11**, 3163-3165.
53 P. Pyykko and M. Atsumi, *Chemistry*, 2009, **15**, 186-197.
54 W. Hu, Z. Li and J. Yang, *The Journal of chemical physics*, 2013, **138**, 124706.
55 W. Hu, T. Wang, R.q. Zhang and J.l. Yang, *Journal of Materials Chemistry C*, 2016, **4**, 1776-1781.
56 Y.-J. Yu, Y. Zhao, S. Ryu, L.E. Brus, K.S. Kim and P. Kim, *Nano letters*, 2009, **9**, 3430-3434.
57 S. Lany and A. Zunger, *Physical Review B*, 2008, **78**, 235104.
58 A. Du, S. Sanvito, Z. Li, D. Wang, Y. Jiao, T. Liao, Q. Sun, Y.H. Ng, Z. Zhu, R. Amal and S.C. Smith, *Journal of the American Chemical Society*, 2012, **134**, 4393-4397.
59 A. Du, Y.H. Ng, N.J. Bell, Z. Zhu, R. Amal and S.C. Smith, *J Phys Chem Lett*, 2011, **2**, 894-899.